Perspective

Performance metrics for shape-morphing devices

Jue Wang ⓘ & Alex Chortos ✉

Abstract

Shape-morphing devices, with their capacity to undergo structural transformations, are on the verge of revolutionizing multiple domains, from human–machine interfaces to biomedical and aerospace applications. This Perspective classifies shape-morphing devices into two categories: pattern-to-pattern shape-morphing devices that deform from a starting shape to a predefined set of one or more deformed shapes, and programmable shape-morphing devices that can morph into different shapes on demand. We highlight the need for standardized assessment approaches to compare the performance of different shape-morphing devices and introduce an array of proposed metrics that are tailored to assess the functionality of these devices at the material, device and system levels. Notably, we propose a mathematical metric to quantify the complexity of a surface and a set of standard surfaces for evaluating programmable shape-morphing devices, providing objective benchmarks for this expanding field.

Sections

School of Mechanical Engineering, Purdue University, West Lafayette, IN, USA. ✉e-mail: achortos@purdue.edu

Perspective

Introduction

Shape-morphing devices are systems that can alter their form or structure. The transformation can be achieved by inducing mechanical deformation through traditional actuators or by using materials that respond to stimuli. The potential of shape-morphing technologies is being explored across a wide range of disciplines, including robotics[1], aerospace engineering[2,3] and architecture[4,5]. The ability to physically transform is valuable for a multitude of applications, such as in adaptive structures[6], self-assembling systems[7], biomedical devices[8–10] and metamaterials[11,12]. Shape-morphing devices need to fulfil three primary criteria: the deformation should be controllable, it should be revertible to its original state and it should have the versatility to achieve various target shapes. In essence, an ideal shape-morphing device should be controllable, reversible and programmable.

Because the field is relatively new, standard metrics for evaluating performance have not been established, making it difficult to compare different devices. In this Perspective, we classify shape-morphing devices into two main categories: pattern-to-pattern shape-morphing (PPSM) and programmable shape-morphing (PSM) devices. We introduce a set of performance metrics and describe the impact of each metric on the performance of the device. Organizing these performance metrics into radar charts provides an intuitive means to visually represent functionality, thereby enabling a more objective comparison between different technology platforms. Furthermore, these radar charts can facilitate matching device types with applications, guide the optimization of device design and inform the selection of materials and actuation methods. In addition, we propose a standard metric for quantifying the complexity of a surface and a set of standard surfaces to better compare the shape-morphing capabilities of different technology platforms. This standard can serve as a guide for future research to quantify the performance of new devices.

Classification of shape-morphing devices

Pattern-to-pattern shape-morphing devices

PPSM devices undergo deformations towards specific predetermined shapes, governed by the structural design and material distribution. The entire structure can be considered as a complete deformation unit. As the structure and materials are determined during fabrication, the possible final shapes are discrete and finite. Attaining a target shape requires the use of inverse design, which is the process of determining the parameters or design elements necessary to achieve a desired shape or function. To facilitate manufacturing and inverse design, much of the work in this field involves deforming an initial flat shape into a 3D shape, known as 2.5D shape morphing[13–15]. In some robotic applications, the transformation from a closed-form 3D shape to another 3D shape is referred to as 3D shape morphing[1,16,17].
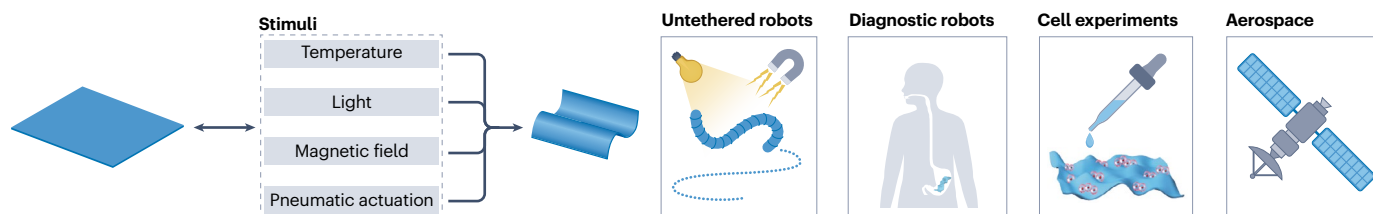
PPSM devices are activated by environmental stimuli, such as temperature changes, or by globally applied stimuli, such as magnetic fields (Fig. 1a). Within the realm of robotics, PPSM devices have been extensively employed in untethered locomotion robots[18–20]. In the biological sphere, PPSM enables diagnostic and drug delivery robots[17,21,22] with transformative potential for in vivo applications. In vitro, PPSM can be employed to guide the assembly of biological systems to achieve specific morphologies[8–10] and to perform mechanobiology experiments[23]. In aerospace engineering, PPSM enables the design of deployable systems that have small collapsed size and weight but can be deployed into larger structures, for example, in the solar sails of satellites[24] and planetary rovers[25]. Finally, structural devices that respond to their environment find application in adaptive architectural frameworks, such as adaptive windows that change shape and transparency in response to temperature and light stimuli[4,26], and responsive systems can be used in textiles to make smart clothes with autonomous thermal regulation[27,28].

Morphing between two specific shapes is accomplished by locally tailoring the response of a structure to an external stimulus. The ubiquitous nature of thermal energy has motivated the development of many thermally activated materials. Temperature-induced deformation is typically largest during the phase transition of a material. For example, the nematic-to-isotropic transition in liquid crystal elastomer (LCE) actuators can result in large temperature-induced strains[29,30]. In hydrogels, thermo-responsive volume changes are driven by a temperature-induced change in solubility that modulates the water content and therefore the volume. This change in solubility is caused by polymer chains transitioning from a coil (or swollen) state to a globule (or collapsed) state at a specific temperature[31–34]. Poly(N-isopropylacrylamide) and its copolymers are the most widely used of these hydrogels. Another way to achieve shape morphing based on temperature change is to use shape-memory materials, such as shape-memory alloys (SMAs)[35] and shape-memory polymers[36–38]. The shape change occurs when the transition temperature at which the material goes through a phase change is reached. Thermal actuators can be activated remotely by light (photothermal activation)[39] if they contain light-absorbing nanomaterials such as graphene[40] and magnetite nanoparticles[41]. Light can also be directly leveraged as an actuation mechanism by using molecules that are sensitive to light exposure. For example, in ordered crosslinked polymers such as LCEs, photo-induced changes in the conformation of molecular additives can disrupt the molecular ordering and induce a phase change[42,43]. Magnetic shape morphing is achieved by embedding ferromagnetic particles within elastomers, such that they respond to the magnetic forces produced upon applying an external magnetic field. The orientation of ferromagnetic particles, combined with the direction of the magnetic field, can dictate distinct deformation patterns[15,44]. Finally, the principle behind pneumatic shape morphing is elegantly straightforward and typically hinges on intricate air chamber designs to achieve controlled and complex shape transformations[14,45]. The resulting devices are robust and reliable, but the use of air chambers prevents miniaturization of this actuation mechanism.

For stimulus-responsive materials, in addition to the material properties, fabrication processes have crucial roles in the complexity of the achieved shape morphing. Laser or wafer-jet cutting[46,47] is efficient for quickly creating intricate patterns, but they are often limited to 2D structures and may have material compatibility issues. Additionally, laser cutting can sometimes cause thermal damage to the material. Lithography offers precise fabrication of structures[48] smaller than those obtained by laser cutting. Lithography is usually limited to flat surfaces and requires specific equipment, but this equipment is generally widely available owing to its use in microelectronics. Three-dimensional printing[15,49,50] and 4D printing[51,52] are popular because they are highly versatile and allow for complex geometries and multimaterial constructs, although they can be time-consuming and may require post-processing. Some responsive materials require stimuli during fabrication to enable the function of the materials. Magnetic particles often need to be aligned using a magnetic field, which has been incorporated into lithography[48] and 3D printing approaches[15]. The polymer chains in LCEs must be aligned during fabrication. Light-induced alignment has been used to prepare 2D surface patterns that were subsequently actuated under an electric field[53]. Three-dimensional

Perspective

a Pattern-to-pattern shape-morphing devices

Stimuli
- Temperature
- Light
- Magnetic field
- Pneumatic actuation

Untethered robots | Diagnostic robots | Cell experiments | Aerospace

b Programmable shape-morphing devices

Control signals
- Discrete
- Continuous

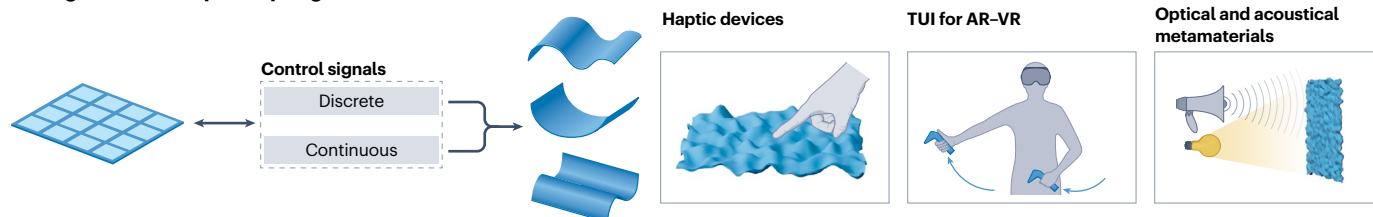Haptic devices | TUI for AR–VR | Optical and acoustical metamaterials

Fig. 1 | Pattern-to-pattern shape morphing and dynamic programmable shape morphing. a, Four common actuation methods for pattern-to-pattern shape morphing (PPSM) are temperature, light, magnetic fields and pneumatic stimuli. PPSM devices can be used, among other applications, in untethered robots, diagnostic robots for use in vivo, in vitro cell experiments and aerospace applications. **b**, The signals controlling the actuation of programmable shape-morphing (PSM) devices can be discrete or continuous. PSM devices can be used in haptic devices, tangible user interfaces (TUIs) for augmented reality (AR) and virtual reality (VR) applications and in optical and acoustical metamaterials.

structures have been created by assembling light-aligned LCE units to create more complex 3D deformations[54]. The mechanical shear forces during 3D printing have been leveraged to align LCE chains along the print path, enabling versatile patterning in complex 3D geometries[50].

The programmability of PPSM devices is rooted in the material, fabrication process and external stimulus used. Therefore, those properties have important roles in determining the performance metrics of PPSM devices. The main limitation of PPSM devices is that they can only morph into a limited number of shapes.

Programmable shape-morphing devices

PSM devices can morph from their initial shape into many different shapes on demand, driven by a stimulus with a spatially controlled magnitude. PSM devices, therefore, require a control system that actively modulates the spatial actuation throughout the device. They allow for a continuous range of infinite morphing possibilities within certain deformation limits (Fig. 1b). Haptic devices are an important field of application for PSM devices. Actuator arrays can be used for 3D tactile displays, as well as in gaming and medical simulators[55]. Advancements in actuator technologies enable the emerging field of immersive haptics, which include augmented reality (AR) and virtual reality (VR). AR and VR devices enhance the immersive experience by emulating touch and physical structure, which are critical from both a social and a cognitive perspective. Tangible user interfaces, designed to physically interact with users, are composed of arrays of actuators made from soft materials, ensuring safe interaction with humans. The design and control of these soft actuator arrays, enabled by shape-morphing technology, are poised to enhance the next generation of AR and VR devices[56]. PSM devices can also be incorporated into metamaterials − materials that possess properties not found in natural structures[57–60] − to enable on-demand tunability of their local properties. For example,

acoustic metamaterials can guide sound waves to create silent areas in loud public places or focus acoustic energy in advanced medical imaging[59]. On-demand tuning of the geometry of the metamaterial enables tunable lenses, filters and modulators, which can dynamically adjust their properties based on the changing needs of the situation[61]. Integrating PSM into mechanical metamaterials would enable changing their damping or stiffness on demand for applications in impact mitigation and lightweighting of high-performance structures[62,63].

The concept of using an array of solid linear actuators to realize shape morphing was introduced during the 1990s and early 2000s. The morphing surface can be described discretely by controlling the height of each actuator. This concept was first proposed by Koichi Hirota and Michitaka Hirose in 1993. They used a 4 × 4 matrix of linear actuators to form custom surfaces[64]. Subsequently, many prototypes, such as FEELEX[65], Relief[66] and inFORM[67], have been developed with higher resolution (more actuators). The actuator mechanisms used in these devices include traditional electric motors, pneumatic linear actuators[68,69], SMAs[70] and dielectric elastomer actuators (DEAs)[71].

Despite these advancements, fabricating PSM devices is still challenging. The expansive matrix of linear actuators is physically large, and the individualized control of each actuator requires a large and complex control system. These issues render the technology challenging to integrate into wearable technologies and microdevices.

Advancements in materials, fabrication technologies and control algorithms have enabled a new class of PSM devices that consist of a continuous surface, driven by low-profile actuator arrays. Distinct from the discrete surfaces in which the actuators are mechanically independent, these continuous surfaces are composed of bending actuators that are mechanically coupled. The first examples of these surfaces consisted of a small number of bending actuators spanning the entire length of the surface, including devices composed of SMAs[72],
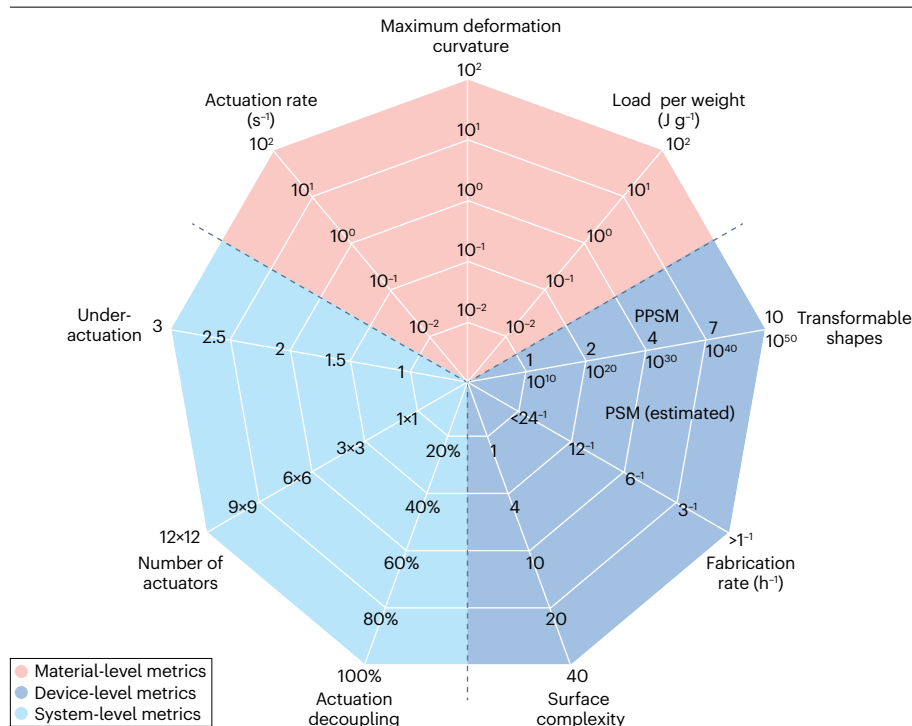
Perspective

pneumatic actuators[73] and LCEs[74]. These devices are relatively easy to fabricate because electrical connections to the actuators can be made at the edges of the surface. However, as the actuators span the whole surface, the shapes that can be produced are limited to simple structures such as a cone or saddle. More complex surface topologies with multiple features can be created when the bending magnitude and direction can be controlled by addressable actuator segments along the dimension of a surface. The key challenge is then to individually address each of the actuating segments. Securing one wire to each side of an actuating segment (direct addressing) is cumbersome and the wiring may impose mechanical constraints that affect the actuation. To address this issue, low-profile magnetic actuator arrays with each side divided into eight controllable actuating segments were designed[75]. The segments were addressed using electrical connections at the edges of the surface. This addressing scheme allowed an N^2 array of actuators to be controlled using $4N$ independent inputs. However, the current through each of the actuator segments was not independent, limiting the surfaces that could be created. Using a crossbar matrix of electrodes instead allows fully independent control of each actuating segment and allows N^2 actuators to be controlled with only $2N$ electrical connections. The capacitor-like properties of ionic actuators were leveraged to create a 6×6 array of actuators that could maintain its actuated state without power[76]. This strategy not only substantially increases the complexity of achievable surfaces but also minimizes the necessary control signals. Finally, although electrically addressed actuators have a multitude of potential addressing methods, pneumatic actuation is typically mediated by electronic controls. For example, a pneumatic equivalent of direct addressing can be accomplished using solenoids to control fluid pressure in an array of actuators[77,78]. Alternatively, a single pneumatic actuator can be controlled to morph into different shapes by incorporating a stiffness-tunable layer that is electrically controlled[79].

For PSM devices, the aim is to achieve a streamlined control system and high 'programmability'. The programmability of a morphing surface has not previously been defined but is intuitively related to how effectively the system can reproduce an arbitrary target surface. Naturally, the inherent performance of the actuator, being a critical attribute of the system, should also be taken into account when evaluating this type of devices.

Performance metrics

The performance of shape-morphing devices includes contributions from three levels: the materials and actuation mechanisms; the device design; and the system-level design and controls. We propose a total of nine metrics distributed across these three levels (Fig. 2). At the material level, metrics refer to the physical properties of the material of the actuator, namely, the actuation rate, maximum deformation curvature and load per weight. Moving to the device level, metrics are related to the shape a device can morph into and aspects of device fabrication, and they are transformable shapes, fabrication rate and surface complexity. The structure of the device, fabrication methods and the type of external stimuli all influence the device-level metrics. For PPSM devices, programmability is achieved through the inverse design of a single actuator without the need to modulate input signals for all actuators or consider coupling within an actuator array. Therefore, PPSM metrics are confined to material and device levels. For PSM systems implemented with actuator arrays, programmability is facilitated through a control system regulating input signals of each actuator in conjunction with coordinated deformation among actuators, necessitating consideration of system-level metrics. These system-level metrics are actuation decoupling, number of actuators and under-actuation. The units and levels for each performance metric are illustrated in Fig. 2, and the performance metrics for some selected

Perspective

examples are shown in Fig. 3. The specific values can change as the field progresses. We provide a detailed definition and explanation of each performance metric in the following sections.

Actuation rate

The actuation rate (material-level metric) measures the reciprocal of the time it takes for the actuators to transition from their initial state to a target state and then back to their initial state. It is a crucial attribute for applications in in vivo diagnostics robots, in which a rapid response is essential. Also, in AR and VR devices and haptic interfaces, a rapid actuation rate ensures real-time or near-real-time interactions, crucial for a seamless and immersive experience. Conversely, this metric may be of lesser significance for applications such as in vitro cell culturing, in which the prolonged duration of cell growth renders the actuation speed less important.

The five points on the radar chart represent 1/100, 1/10, 1, 10 and 100 s^{-1}, respectively. Actuators driven by magnetic fields[15,75,80,81] and electrostatic fields[79,82] are characterized by real-time responsiveness, with response times of the order of milliseconds. They provide the highest actuation rates of 10–100 s^{-1}. Pneumatic actuators[14,73,83–85]

exhibit a slightly delayed response owing to flow rate factors. Their actuation rate is usually 1–10 s^{-1}, so they are still able to achieve real-time performance. Thermal actuators, such as SMAs[72], materials with different thermal expansion coefficients[51] and LCEs[74], may exhibit fast heating phases of less than a second, but their cooling phases tend to be more protracted. Depending on their working environment, thermal conductivity and contact area with the environment, their overall actuation rate ranges from 1/100 s^{-1} to 1 s^{-1}. Ionic actuators, operating on principles reminiscent of ionic capacitive charging and discharging processes, tend to be slower, necessitating several seconds to tens of seconds for a full-loop actuation[76], which results in an actuation rate of 1/100–1/10 s^{-1}.

Maximum deformation curvature

The maximum deformation curvature (a material-level metric) refers to the highest curvature achieved by a single actuator within a shape-morphing device. The maximum deformation curvature is a critical factor influencing the complexity of the final deformation of the device. Higher localized curvature can result in a greater overall magnitude of the deformed shape. This is particularly important for specific
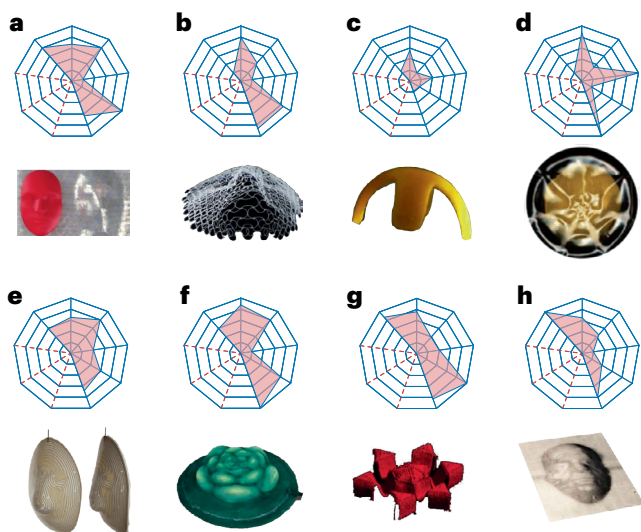

Fig. 3 | Performance metrics of selected shape-morphing devices.
a, Jamming skin that can replicate the shape of objects owing to its tunable stiffness[83]. **b**, Pattern-to-pattern shape-morphing (PPSM) device fabricated by 4D multimaterial printing and assembled by bending lattices with high surface complexity and thermally actuated[51]. **c**, Hydrogel-based shape-morphing device driven by synergistic stimuli with fast response[19]. **d**, Photo-induced PPSM device with multiple deformation patterns under different light wavelengths based on liquid crystal elastomer networks[91]. **e**, Pneumatic PPSM device designed by inverse design with high surface complexity[14]. **f**, Pneumatic PPSM device based on bulking deformation with fast inverse design and fabrication[84]. **g**, Three-dimensional-printed magnetic-driven PPSM device with fast response and high surface complexity[15]. **h**, High surface complexity PPSM device made by architected dielectric elastomer actuators with an inverse design strategy[82]. **i**, The earliest programmable shape-morphing (PSM) design based on a bilayer of shape-memory alloys showcasing a square mechanism[72]. **j**, Shape-changing membrane enabled by six tensile jamming fibres[73]. **k**, A closed-form PSM device with 19 independent jamming chambers[85]. **l**, PSM device that employs liquid crystal elastomer bending actuators, consisting of three actuators oriented along each
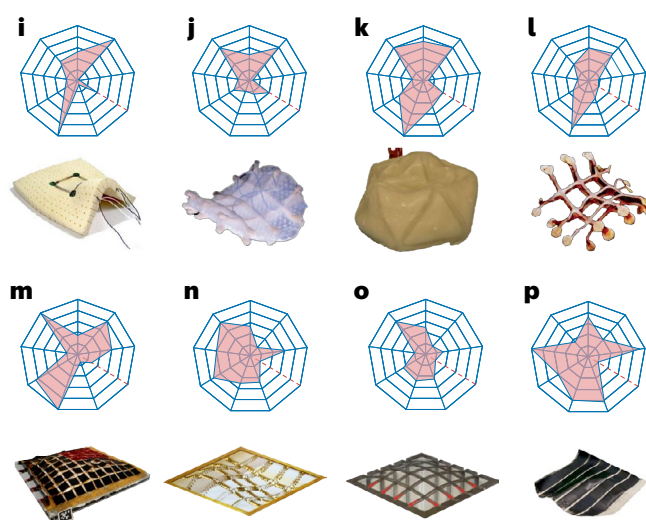
of two orthogonal directions[74]. **m**, PSM device rooted in electrostatic adhesion principles, achieving surface shape control via a 10 × 10 stiffness-tunable array[79]. **n**, 4 × 4 interconnected liquid metal networks driven by the Lorentz force of magnetic field[80]. **o**, PSM device driven by the Lorentz force from magnetic fields, comprising 4 × 4 (potentially scalable to 8 × 8) interconnected, serpentine-shaped beams made of thin conductive layers[75]. **p**, PSM device addressed by a passive matrix made by 6 × 6 ionic actuator arrays based on machine-learning control[76]. Panel **a** adapted with permission from ref. 83, Wiley. Panel **b** adapted with permission from ref. 51, PNAS. Panel **c** reprinted with permission from ref. 19, AAAS. Panel **d** adapted with permission from ref. 91, Wiley. Panel **e** reprinted from ref. 14, Springer Nature Limited. Panel **f** reprinted with permission from ref. 84, AAAS. Panel **g** reprinted from ref. 15, Springer Nature Limited. Panel **h** reprinted with permission from ref. 82, AAAS. Panel **i** reprinted with permission from ref. 72, ACM. Panel **j** reprinted with permission from ref. 73, AAAS. Panel **k** reprinted with permission from ref. 85, IEEE. Panel **l** reprinted with permission from ref. 74, AAAS. Panel **m** reprinted with permission from ref. 79, IEEE. Panel **n** reprinted from ref. 80, CC BY 4.0. Panel **o** reprinted from ref. 75, Springer Nature Limited. Panel **p** reprinted with permission from ref. 76, AAAS.

Perspective

applications such as drug delivery, in which the shape-morphing device must achieve a sufficiently high maximum deformation curvature to completely envelop the drug and ensure effective delivery. This metric can be quantified by the angular change accomplished by a single actuating unit, which is the length of the actuator divided by the radius of the curvature (arrange the equation for arc length to solve for the angle), giving a unitless value. For a PPSM, the size of the actuator is the full device, whereas for a PSM, it is one pixel. For example, in our recent work[76], the smallest radius of bending of our ionic actuator was about 9 mm, whereas the total size was 54 mm, giving a maximum deformation curvature of 6 after normalizing the total size to 1. The values represented by the 5 points on the radar chart are curvature values of 1/100, 1/10, 1, 10 and 100.

This metric is closely related to the deformation mechanism of the actuator. Bending (including folding in origami mechanisms) and buckling are the two predominant deformation mechanisms in actuators. Materials with volumetric change, such as LCEs[74] and hydrogels[19,31], when combined with a passive layer can achieve bending. The migration of ions inside ionic actuators generates a volume change at the top and bottom electrodes, which can cause bending[76]. The maximum bending curvature of such a laminated bending actuator is primarily influenced by the properties of the material, the strain change of the material in different phases and the thickness and modulus of each layer. Deformation is also possible with magnetic-driven actuators[15,48], in which the torque produced by a magnetic field can directly induce bending. When stimulation produces compressive forces on a structure, buckling can occur. In appropriate geometries, buckling can be produced by pressure in a pneumatic actuator[14,84], the electrostatic force in a DEA[82] or swelling of hydrogels[86,87]. For actuators that operate on a buckling principle, factors such as the elastic modulus of the material, geometric parameters and boundary conditions determine the maximum deformation curvature.

Load per weight

The load per weight metric (material-level metric) reflects the load-bearing capacity of an actuator. Some applications of shape-morphing devices require the application of forces, such as space robotics and devices for in vivo medical interventions. If a shape-morphing device has low force output during transformation, then its usage is largely confined to applications such as 3D displays or acoustic metamaterials.

For this metric, we use the energy density, which can be quantified by the output work generated by the actuator normalized to its mass. The five points on the radar chart represent 1/100, 1/10, 1, 10 and 100 J g^{-1}.

SMAs[72,88] have the highest energy density among all common actuators, approaching 100 J g^{-1} (ref. 89). The energy density generated by a pneumatic actuator, including inflating[14,77,84] and jamming[73,83,85], is directly related to the air pressure. With robust designs and high pressures, these actuators can achieve substantial energy densities of around 10 J g^{-1}. LCEs[48,74] can reach an energy density of ~10 J g^{-1}, but this value can vary widely from 1/10 to 10 based on the molecular alignment and phase transition properties[90]. When DEAs are well optimized, they can exhibit an energy density of about 1 J g^{-1} (ref. 82), although general DEAs range between 0.1 J g^{-1} and 1 J g^{-1} (ref. 89). Ionic actuators, owing to their deformation principle stemming from the migration of ions under the drive at a lower voltage, possess a lower energy density. However, given their light weight, their load per weight ratio can be around 0.1 J g^{-1} (ref. 89). Magnetic actuators[15,75,80,81] have relatively low energy density, ranging from 0.01 J g^{-1} to 0.1 J g^{-1}. Their force depends on the strength of the external magnetic field and the density and/or orientation of magnetic particles. Hydrogel actuators[19,31] generally come in last compared with the previously mentioned actuators, often having energy densities of less than 0.01 J g^{-1}, thus they can typically only load their own weight.

Transformable shapes

For PPSM devices, transformable shapes (device-level metric) refer to the number of different transformation patterns a single prototype can exhibit. Although the structure of a PPSM device is defined during fabrication, some responsive materials or structures can exhibit different responses to different types of stimuli, enabling a single PPSM device to morph into different structures depending on the stimulus. The device can then be used for various assignments without the need for redesign or remanufacture. Transformable shapes have limited impact on applications of PPSM devices that perform only one task, such as drug delivery capsules or solar panels on satellites. However, for locomotion robots, in which movement patterns or directional changes necessitate multiple transformable shapes, or for adaptive optics, in which an optical component must perform various functions, transformable shapes become a crucial metric.

As the number of transformable shapes for PPSM devices is discrete and finite, the number of shapes can be directly used as the metric: 1, 2, 4, 7 and ≥10. For instance, incorporating light-sensitive moieties into LCEs enables materials that have different shape-morphing characteristics based on the wavelength of light, enabling more than 10 different shapes from one PPSM device[91]. For devices driven by a magnetic field, reversing the field direction can provide multiple deformation patterns[15,48]. Pneumatic-driven shape-morphing devices can exhibit two different transformation patterns under positive and negative air pressure[14], but jamming devices, after their shape is passively determined by an external rigid object, can only tune their stiffness[83]. For materials whose properties depend only on the magnitude of the stimulus (such as DEAs[82] and heat-induced LCEs[51]), a device can only morph into a single predetermined shape.

For many of the potential applications of PSM devices, the most crucial attribute is the ability to change into a wide range of shapes, making the number of transformable shapes an important metric. PSM devices with actuator arrays deform into different shapes, depending on the control input distribution. If each actuator can achieve a continuous range of deformation states through control signals, it theoretically possesses infinite combinations of control inputs, allowing for an infinite variety of transformable shapes. In this case, the deformation capabilities of a single actuator and the number of actuators determine the range of transformable shapes. Actuators such as SMAs[72,88] and electroadhesion actuators[79], which only have two states (on and off), have theoretically finite transformable shapes. However, the number of shapes the device can achieve is still remarkably larger than that for PPSM devices.

To enable a comparison between theoretically infinite and finite transformable shapes, we assume that actuators with unidirectional continuous control inputs, such as thermal actuators or DEAs, have 10 statuses, and those with bidirectional control input have 20 statuses. On the basis of these definitions, we can quantify this metric for PSM devices. For example, a device composed of 36 independently drivable bidirectional continuous bending actuators[76] has 20^{36} potential combinations of control signals (based on our assumptions), which is the highest among all sampled papers, resulting in the largest range of transformation shapes. For a device with 32 control units with

Perspective

only positive inputs (unidirectional)[75], the number of transformable shapes is 10^{32}. For a similar device with 16 independent positive control inputs[80], the estimated number of transformable shapes is 10^{16}. For a device containing 6 independently controllable bidirectional continuous bending actuators[74], the value of transformable shapes is 20^6. For devices that contain actuators that have only two states[72,73,85], on and off, their number of transformable shapes is 2^n, in which n is the number of independent control inputs. For a large array of these on–off actuators[79] (10×10), the transformable shapes can be 2^{100}, which is between 10^{16} and 10^{32}, the limits of the range for actuators with unidirectional continuous bending. On the basis of these examples, our radar chart uses increments of $0, 10^{10}, 10^{20}, 10^{30}, 10^{40}$ and 10^{50}.

Fabrication rate

Fabrication rate (device-level metric) refers to the speed at which a new prototype is manufactured, with higher rates translating to less time needed per prototype. Fabrication rate is less important for high-value applications of PPSM devices in which only one device is used, such as deploying solar panels of satellites. Fabrication rate becomes a critical factor for PPSM devices in which new devices may need to be fabricated regularly to meet changing application requirements, such as decorations and displays[84], multifunctional robots[15] and patient-specific medical devices[92]. The ability to swiftly manufacture devices according to the demanded shapes is vital for the industrialization of these applications. To quantify this metric, we evaluate it based on the active hours required by researchers using different fabrication methods, which is related to the level of automation. As a metric, we use the reciprocal of active hours, with increments of 1/24, 1/12, 1/6, 1/3 and 1/1 h.

Although the fabrication rate of 3D printing is low compared with conventional manufacturing approaches (such as injection moulding and slot coating), this is the fastest method to prototype different structures. Thus, 3D[15] and 4D[51] printing techniques often require the least active time of researchers (1/2–1/0.5 h), resulting in the highest fabrication rates for shape-morphing devices. UV lithography[48] and laser cutting[84] mirror the efficiency of 3D printing, yet it typically necessitates additional steps to finalize the fabrication of the mechanism, resulting in a slightly reduced fabrication rate (1/3–1/1 h). Mould-based fabrication[14] excels in the rapid replication of identical structures; however, crafting different structures demands distinct moulds, rendering its fabrication rate marginally lower than that of 3D printing (1/12–1/3 h). Thin-film fabrication[19,31,82,91], a manual laboratory-centric method, is time-intensive from the material preparation to the fabrication of multiple layers and cannot be automated, hence registering the lowest fabrication rate (1/24–1/6 h).

In PSM devices, the programmability arises from the distribution of control inputs. Morphing into a different shape requires only changing the control inputs, without needing to design a new device. Thus, fabrication rate does not affect the day-to-day utility of a PSM device. Consequently, fabrication rate mainly affects the fabrication cost of the devices. Although PPSM devices consist of patterned materials and can hence be fabricated in automated ways, PSM devices consist of complex assemblies including multiple actuators and controls and are currently assembled manually in the laboratory. Consequently, fabrication rate is not typically reported for PSM devices, but will become a more important consideration as the field matures and approaches commercialization.

Surface complexity

Surface complexity (device-level metric) serves as a measure of the morphing capabilities of a device and reflects its potential applicability across various scenarios. In the case of PPSM devices, surface complexity is influenced not only by the material metrics of the actuator but also by the structural design of an actuator and by the external stimuli applied. Robots with low surface complexity are suitable for basic actions such as grasping and simple locomotion. By contrast, higher surface complexity enables applications in advanced locomotion, such as the undulating motion used by some underwater animals, and in physical displays and other human interfaces. For PSM devices, although the device design remains constant, the characteristics of the control system and the interactions between actuators emerge as important factors beyond material metrics that impact surface complexity. Achieving sufficiently complex surfaces is fundamental for PSM to be applicable in 3D displays, robotics, AR–VR devices and so on.

Currently, there is no universally accepted metric to evaluate the complexity of a surface. Consequently, we introduce here a new quantitative assessment of surface complexity based on the variation in normal vectors. This evaluation method gives a higher score to devices with greater curvature and more variation in curvature. Specifically, shapes exhibiting pronounced deformation magnitudes or possessing detailed local features receive higher scores. By contrast, shapes with larger resolution, smoother overall appearance and limited deformation are scored lower.

The specific computation process is as follows. Initially, we generate a mesh across the surface, whose density depends on the necessary level of detail. For example, the local deformation features of PSM devices are often about 1/10 to 1/3 of their overall size. Therefore, we set the mesh granularity to 30×30. Each vertex in this grid is associated with a normalized 3D normal vector $\mathbf{n} = (n_x, n_y, n_z)$. Subsequently, for each normal vector, we compute the angle θ it forms with its immediate neighbours along the grid ($\mathbf{n}_1, \mathbf{n}_2, \mathbf{n}_3, \mathbf{n}_4$) in the x and y directions (Fig. 4a). Next, we collect all the angles θ and flatten them to a long vector. Then, we compute the variance of the angle vector, which serves as a measure of the dispersion or complexity of angle variations across the surface. A smaller variance implies a more regular or smoother surface with a lower deformation magnitude, whereas a larger variance suggests a more complex surface or a surface with more details with a larger deformation magnitude. Compared with calculating the variance of Gaussian curvature on all nodes, this method results in smoother changes without noticeable jumps; in contrast to calculating the variance of mean curvature on all nodes, dual shapes (such as surfaces $z = 0.2\cos(4\pi x)\cos(2\pi y)$ and $z = 0.2\cos(2\pi x)\cos(4\pi y)$) yield identical results, which aligns with our intuitive understanding of surface complexity. Consequently, through comparing the variance values of distinct surfaces, we can effectively quantify their relative complexities in a standardized way.

For example, with a mesh of 30×30, for standard shapes such as a dome $z^2 = x^2 + y^2$ (Fig. 4b) and a saddle $z^2 = x^2 - y^2$ (Fig. 4c), the variance of the normal vectors is the same, 0.468. This implies that these two standard shapes have equivalent surface complexity. If the shapes of these two surfaces remain constant, but their deformation increases ($z^2 = 2x^2 + 2y^2$, $z^2 = 2x^2 - 2y^2$), their variance increases to 2.374 (Fig. 4d,e). This observation aligns with common sense: a similar shape with larger deformation should indeed possess higher surface complexity. If the surface gradually becomes more varied and detailed, for instance, $z = 0.2\cos(2\pi x)\cos(2\pi y)$ (Fig. 4f) and $z = 0.2\cos(4\pi x)\cos(4\pi y)$ (Fig. 4g), the variance increases substantially to 10.857 and 122.789, respectively. In addition, when it comes to more irregular surfaces such as $z = 0.2\sin(12xy)\sin(14xy)$ (Fig. 4h) and $z = 0.2\sin(5x)\cos(5y) + 0.6\exp(20(x^2 + y^2))$ (Fig. 4i), the variance

Perspective

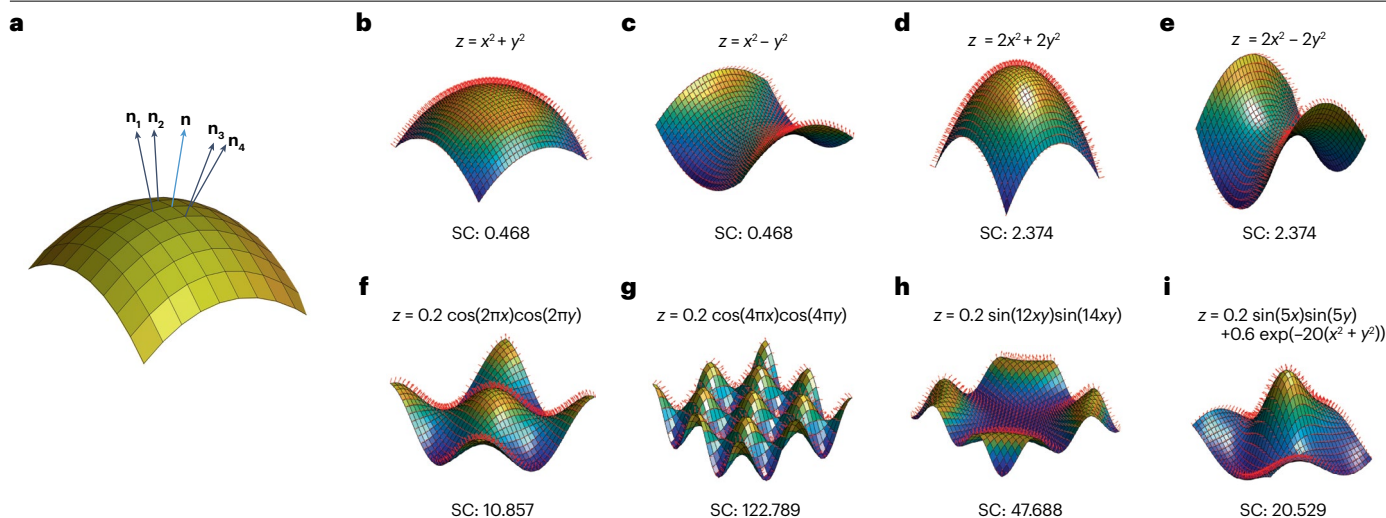**Fig. 4 | Method to evaluate surface complexity. a**, Definition of surface complexity (SC) based on the variation of normal vectors. **b,c**, Standard dome (part **b**) and saddle (part **c**) surfaces with the same SC of 0.468. **d,e**, Dome (part **d**) and saddle (part **e**) surfaces with a larger deformation magnitude increase the SC to 2.374. **f**, A surface with a complete cosine cycle in both the x and y directions has an SC of 10.857. **g**, A surface with two complete cosine cycles in both the x and y directions has an SC of 122.789. **h,i**, Two random surfaces with SCs of 47.688 and 20.529, respectively.

becomes 47.688 and 20.529, which aligns with our intuitive perception of surface complexity.

Given that this performance metric is introduced here for the first time, the values in the radar charts in Fig. 3 are estimates based on the final deformation shapes demonstrated in these works. The five levels in the radar chart are 1, 4, 10, 20 and 40. This measure of surface complexity could provide a useful tool to objectively evaluate the deformation capability of future shape-morphing devices.

Actuation decoupling

Actuation decoupling is a system-level metric that is only relevant to PSM devices, which possesses arrays of actuators that may interact with each other. This metric reflects the extent to which each actuator can be independently controlled. Actuation decoupling is of crucial importance for PSM devices owing to its direct impact on the complexity of the surfaces that can be achieved. When each actuator can operate independently, it is possible to tailor the movement and deformation of each small section of the surface, allowing for surfaces with more detailed structures. Therefore, actuation decoupling has an important role in display-related applications.

We propose quantifying the actuation decoupling using the crosstalk in the control signal (voltage for DEA and ionic actuators, pressure for pneumatic), which is the percentage error between the actual input and target input applied to each actuator. Crosstalk is typically not discussed in shape-morphing papers, but here we propose a method for quantifying actuation decoupling, enabling future work to follow a standardized approach. We propose defining the actuation decoupling as the average of the crosstalk across all actuators, as described subsequently.

A standard control signal, X, is applied to the central actuator, and the actual control inputs, X_j, for the other actuators are measured. For actuators under indirect control, the parameters of directly controlled actuators should be considered as the input signal. For instance, in the case of an electrically driven thermal actuator, the central

actuator should be regulated to achieve a standard temperature X, and then the temperature inputs X_j on other actuators should be measured. Subsequently, we calculate the average of all X_j values and normalize this by dividing it by X. This quotient represents the crosstalk level, which directly indicates the actuation decoupling within the PSM device. The specific equation is

$$\text{Actuation decoupling} = 1 - \text{crosstalk} = 1 - \frac{1}{X} \cdot \frac{\sum_{j=1, j \neq i}^{N} X_j}{N-1}.$$

Given that the lack of discussion of the issue of crosstalk in the majority of published works, and the inability to estimate this metric through the visuals provided in the papers, we discuss crosstalk by comparing the underlying physics of different addressing methods. Actuators under the direct control of direct addressing[77,79] individually receive an independent control signal, thereby eliminating the issue of crosstalk (Fig. 3k,m). Consequently, these devices attain the maximum score for this metric, 1. Conversely, for devices employing actuators under indirect control via direct addressing, such as electric-driven thermal actuators[72,74], the absence of electrical crosstalk does not preclude the influence of thermal crosstalk on actuation. Although the thermal crosstalk can be minimized with proper structural design, it is acknowledged that the actuation decoupling cannot achieve a perfect value of 1, but can only approximate it (Fig. 3i,l). In a device using a control algorithm based on passive matrices that allows independent control of each actuator[76], based on the presented passive addressing results, the system exhibits some degree of crosstalk. The actuation coupling resulting from crosstalk is around 10%, which does not notably impact the final actuation. The actuation decoupling value we derive from the definition mentioned earlier is about 0.9 (Fig. 3p). In tomographic magnetic-driven mechanisms[75,80], owing to Kirchhoff's current law, the current through neighbouring conductive segments cannot be independent, necessitating the introduction of feedback for

Perspective

iterative control[75]. On the basis of this fundamental inability to decouple the actuating elements, we estimate a decoupling value of 0.7–0.8 (Fig. 3n,o). Reported PSM devices based on tensile jamming[73] have three tensile strips on each of the top and bottom layers, and all three tensile strips in each layer are either simultaneously actuated or not, with no independent control. Therefore, actuation decoupling of this device is the lowest, 0.6, among the selected examples (Fig. 3j). Considering that the lowest actuation decoupling based on the algorithm proposed in this paper is 0.6, we have established the increments on the radar chart as 0.6, 0.7, 0.8, 0.9 and 1.0.

Number of actuators

Number of actuators (system-level metric) is one of the key metrics that influence the surface complexity in PSM devices (the practical realization of surface complexity is also affected by actuation coupling). The number of actuators remarkably influences the control interface (how the control system delivers stimuli to the actuators). For a system with merely four actuators[72], directly addressing each actuator with individual wires does not pose a substantial burden on the system (Fig. 3i). However, for large-scale arrays with $N \times N$ actuators, $2N \times N$ wires are needed for direct addressing. A large number of connecting wires can result in a bulky control system and affect the deformation capabilities, limiting the application value. To organize these connection wires and facilitate connections to control circuits, flexible printed circuit boards were used to address a 10×10 actuator array[79] (Fig. 3m), with the limitation that the boundaries of the array must be fixed. For systems with a large number of actuators, approaches are being sought to reduce the number of control inputs, such as tomographic addressing[75,80] (Fig. 3n,o) and passive addressing[76]. Passive addressing uses a crossbar array of electrodes to address pixels, with the limitation that electrical crosstalk is unavoidable and increases as the array size increases. Active matrices employ semiconductor devices, such as transistors, in each pixel to eliminate crosstalk. Active matrices are standard technologies for traditional rigid displays such as liquid crystal display screens, which can achieve array sizes with millions of pixels. The recent development of flexible[93,94] and stretchable[95] active matrices could be an enabling technology to scale towards large arrays of actuators.

This metric can be accurately quantified; therefore, the number of actuators can directly be used as the metric. The values corresponding to the 5 points on the radar chart are respectively 1×1, 3×3, 6×6, 9×9 and 12×12. The largest number in our chosen examples is 10×10, and achieving 12×12 is entirely feasible with current technology.

Under-actuation

Under-actuation (system-level metric) quantifies the ability of a system to work with fewer control parameters than degrees of freedom. The degree of under-actuation is quantified as the ratio of outputs (in this case actuators) to inputs (controllable electrical parameters)[96,97]. For PSM devices composed of an actuator array, the prevalent direct addressing scheme[73,74,77,79] necessitates a substantial number of wires and control units. This spatial requirement renders the control system bulky, thereby limiting its viability in portable or wearable devices. We can use the ratio of the number of independently controllable actuators (or pixels) to the number of control inputs to quantify this metric. Among the devices we analysed, the highest ratio of outputs to inputs is achieved by exploiting the properties of an ionic actuator[76] that resemble the charging and discharging of capacitors (when the actuator is subjected to a voltage and subsequently placed in a floating state, it can maintain its deformation). This approach led to the first

application of passive addressing on an actuator array, resulting in an under-actuation system with a ratio of $N^2/2N$, which is $36/120 = 3$ in this case (Fig. 3p). The PSM devices driven by the Lorentz force have $4N$ input to dynamically adjust the current distribution across an N^2 mesh[75,80], in theory, realizing an under-actuation of $N^2/4N$. For 4×8 inputs[75], the score is $64/32 = 2$ (Fig. 3o), whereas the score is $16/16 = 1$ when there are 4×4 inputs[80] (Fig. 3n). However, given that the control of each pixel is not entirely decoupled, the effective under-actuation is lower. The remaining mechanisms rely on direct addressing, wherein the number of control units matches the number of actuators, resulting in the minimum score 1 for these approaches. The maximum value on the radar chart corresponds to the current system with the highest ratio[76], 3, and the minimum value corresponds to 1 for all PSM systems based on direct addressing. Thus, the number for all levels are 1, 1.5, 2, 2.5 and 3.

Selected PPSM devices for proposed performance metrics

In addition to the quantifiable performance metrics we discussed (Fig. 3), Table 1 summarizes some of the non-quantifiable characteristics of PPSM devices that can influence the choice of technology platform for a target application. The deformed shape is determined by the original fabricated shape. Consequently, inverse design is valuable to determine the shape that must be fabricated to accomplish a target deformation. The deformation mechanism influences the scope of attainable shapes, whereas the chosen stimuli determine the conditions or environments under which the devices can operate. The fabrication method determines the types of starting geometries that are possible and the capability for bespoke production and scalability. On the basis of the aforementioned performance metrics and non-quantifiable characteristics, we conducted a detailed analysis of selected examples of PPSM devices.

Figure 3a[83] shows a device utilizing pneumatic jamming principles, resulting in excellent performance in actuation rate and load per weight, making it ideal for adaptive furniture applications requiring high load capacity. The device passively morphs to match the shape of an external object, with the complexity of this object dictating the deformation complexity. However, owing to the resolution limits and the jamming mechanism, the achievable surface complexity is constrained. We evaluate fabrication rate based on the time needed to create a new mechanism from an existing foundation. Thus, shaping the device with an external object is viewed as fabricating a new device, giving it a high fabrication rate. Once the shape of the external object is set, the number of transformable shapes is fixed at one.

Figure 3b[51] showcases a device based on multimaterial 3D printing combined with an impressive inverse design method that controls the deformed shape by manipulating the printing path. The deformation mechanism relies on global heat stimuli to induce a shape change in elastomers with different thermal expansion coefficients. This approach allows for high maximum deformation curvature per actuator and notable overall surface complexity. However, the deformation principle results in limited actuation rate and load per weight. On the basis of these performance metrics, the researchers who fabricated the devices identified and demonstrated promising applications in frequency-shifting antennas and dynamic optics.

Figure 3c[19] presents a device based on Ni nanowires embedded in hydrogels that achieves synergistic actuation through light and magnetic fields. Although the actuator achieves a high maximum deformation curvature, its simple structure results in low surface complexity. The material properties of the hydrogel contribute to a low

Perspective

Table 1 | Non-quantifiable characteristics of pattern-to-pattern shape-morphing devices

Inverse design	Deformation mechanism	Stimulus	Fabrication method	Potential application	Ref.
Yes	Jamming	Pneumatic	Manual in laboratory	Adaptive furniture	83 (Fig. 3a)
Yes	Bending	Heat	3D print	Frequency-shifting antennae	51 (Fig. 3b)
No	Bending	Light–magnetic	Manual in laboratory	Targeted drug delivery	19 (Fig. 3c)
No	Buckling	Light	Manual in laboratory	Advanced optics	91 (Fig. 3d)
Yes	Buckling	Pneumatic	Mould	Minimally invasive surgery	14 (Fig. 3e)
Yes	Buckling	Pneumatic	Laser patterning	Synthetic camouflaging skins	84 (Fig. 3f)
No	Folding	Magnetic	3D print	Reconfigurable soft electronics	15 (Fig. 3g)
Yes	Buckling	Electrostatics	Manual in laboratory	Advanced optics	82 (Fig. 3h)
No	Bending	Light	Manual in laboratory	Flexible electronics	42
No	Buckling	Joule heating	Mould	Medical stents	31
No	Bending–buckling	Joule heating	Manual in laboratory	Wearable electronics	29
No	Bending	Magnetic	UV lithography	Targeted drug delivery	48
No	Bending	Joule heating	Manual in laboratory	Pipeline inspection robot	16
Yes	Bending–twisting	Global heat	4D print	Smart textiles	52
Yes	Folding	Global heat	3D print	Reconfigurable robots	50
No	Bending–folding	Global heat	3D print	Responsive textiles	37

load per weight. However, the incorporation of Ni nanowires enhances the actuation rate compared with other hydrogel devices. The authors did not propose any inverse design methods. Changes in the magnetic field enable various transformable shapes for locomotion and grasping actions, but the device also shows potential for future applications in drug delivery.

Figure 3d[91] illustrates the use of light-induced techniques to create complex surfaces on liquid crystal polymer networks. This device exhibits excellent deformation performance, in terms of both local maximum deformation curvature and overall surface complexity. By varying defect intensities within a single device, different surfaces can be generated, resulting in the highest number of transformable shapes among all PPSM examples. However, the actuation properties of the material, specifically actuation rate and load per weight, are suboptimal, limiting its applications to scenarios that do not require large force output, such as physical displays or advanced optics.

The device in[14] Fig. 3e was fabricated using an inverse design method based on biomimetic principles for traditional pneumatic devices, enabling them to morph into a target shape. The pneumatic mechanism provides excellent actuation performance in terms of actuation rate and load per weight. Additionally, the anisotropic expansion or contraction of the complex internal chambers of the device allows for two distinct deformation modes. However, owing to the buckling-based deformation mechanism, the maximum deformation curvature and surface complexity are limited. Therefore, further research is needed to explore its practical applications in aerospace and minimally invasive surgery.

Figure 3f[84] presents a morphing surface utilizing materials with varying stretchability to achieve an inverse design. Although it also uses a pneumatic actuation mechanism, its structure leverages buckling to generate greater maximum deformation curvature. The use of laser cutting as a rapid manufacturing method enables quick production of new designs and results in high-resolution patterns, leading to a deformed shape with high surface complexity. However, it only allows for inflation-based deformation, limiting the transformable shape to one. This drawback does not affect the target application of synthetic camouflaging skins and flexible displays.

Figure 3g[15] depicts a device driven by internal magnetic torques, which demonstrates excellent performance in actuation rate and maximum deformation curvature, crucial for targeted drug delivery applications. However, it cannot generate sufficient load to carry heavy objects. The use of 3D printing for fabrication not only allows for intricate details that enhance surface complexity but also remarkably reduces the time cost of redesigning a new device. Different magnetic field orientations can produce various transformable shapes, potentially benefiting locomotion-related applications.

Figure 3h[82] demonstrates a device fabricated to replicate a human face by controlling the local actuation direction through 3D printing rigid rings with varying geometries on the surface of a DEA. Additionally, local actuation magnitude is controlled by designing multilayer structures and varying the number of interleaved electrodes, showcasing large surface complexity. The high actuation rate and excellent maximum deformation curvature of the DEA make it suitable for applications requiring rapid and complex shape shifting. However, each device is limited to a single target shape, necessitating the customization of different devices for varied applications. The authors propose a reliable inverse design method based on the target shape utilizing a combination of 3D printing and thin-film fabrication techniques, presenting a relatively rapid strategy for customizing devices.

Selected PSM devices for proposed performance metrics
For PSM devices, Table 2 shows their non-quantifiable characteristics and potential applications. The ability to achieve inverse control is critical for practical use. Among the three main features of shape morphing, controllable refers to inverse control, meaning the capacity to shape the mechanism to achieve a target shape. Continuous and

discrete are the two primary branches in this field. Discrete arrays are more controllable but have larger and more complex control systems. Continuous arrays are more compact but typically have smaller actuation forces and are more challenging to control owing to coupling between pixels. Solving these challenges with continuous arrays is currently the most active area in PSM research. The feedback control is an advanced characteristic in this domain; its integration can enhance the precision of shape replication. For discrete PSM, feedback control is typically embedded within the actuator. By contrast, continuous PSM often relies on smart materials, necessitating external sensors to establish feedback control[96]. We highlight key features of PSM devices subsequently.

Figure 3i[72] showcases a mechanism based on a 2 × 2 bilayer of SMAs, representing the first transition from discrete to continuous PSM. As an early work in PSM development, it lacks a clear application direction. Although SMA performs well at the material level, the limited number of independent actuators prevents the creation of complex surfaces and multiple transformable shapes. Additionally, the control method is the basic direct addressing approach without closed-loop control. Although this avoids actuation coupling, it also does not employ any under-actuation strategies.

The device in[73] Fig. 3j features a pneumatic jamming system with six stiffness-tunable tensile strips. Despite having six strips, it only has two independent control inputs, resulting in a value of 0.6 for actuation decoupling. The open-loop direct addressing control method lacks advantages in under-actuation, leading to low surface complexity and limited transformable shapes. However, the material properties are similar to those of other pneumatic jamming systems, providing excellent actuation rate and load capacity. Therefore, this device is most suitable for applications requiring adaptive surfaces with load-bearing capabilities.

The device in[85] Fig. 3k also employs a pneumatic jamming actuation mode but features 19 independently controlled actuators using direct addressing. This configuration offers advantages in surface complexity and transformable shapes compared with the previous example. Additionally, its unique 3D closed-form structure enables deformation-based locomotion, making it suitable for applications such as pipeline inspection robots.

Figure 3l[74] shows a device using LCE bending actuators, consisting of three actuators aligned along each of two orthogonal directions. Owing to the excellent load-to-weight ratio of LCEs, the deformation remains largely unchanged under heavy loads. However, the temperature-induced actuation limits the actuation rate, restricting applications to scenarios requiring slow deformation with high load capacity. In terms of control, this device lacks feedback mechanisms or any under-actuation strategies. The deformation is entirely governed by the open-loop input to the six actuators. Consequently, the system can only achieve basic shapes, such as domes, saddles and cylindrical surfaces, resulting in lower performance in transformable shapes and surface complexity.

Figure 3m[79] shows a device made of electromagnetic adhesion actuators. As these actuators cannot produce actual deformation, the deformation is achieved through a pneumatic actuator beneath them, combined with the stiffness distribution generated by the array of electromagnetic adhesion actuators. This system has the highest number of actuators among all selected examples, each capable of individual control. However, as each actuator can only perform on–off control, the number of transformable shapes is limited compared with continuously driven actuator arrays. The material properties are

primarily determined by the pneumatic actuator, which is the main source of deformation. Although the system lacks an under-actuation strategy, its flexible printed circuit board control system is not bulky, suggesting potential applications in wearable devices and portable tactile devices once the system is miniaturized.

Figure 3n[75] introduces a mechanism driven by the Lorentz force from magnetic fields, used in a device consisting of a 4 × 4 array of interconnected, serpentine-shaped beams made of thin conductive layers, with the potential to scale up to 8 × 8. The mechanism exhibits a high actuation rate but has a very low load per weight. The control system employs $4N$ inputs to control $N2$ nodes, representing an under-actuation strategy. However, the inputs to each node are coupled with those of other nodes, meaning that the actuation is not fully decoupled, preventing an actuation decoupling score of 1. This device uses a stereo camera system for visual feedback to compensate for modelling errors, achieving high-frequency, dynamic inverse control. Despite this, the coupling between actuators and their small maximum deformation curvature limit the level of local detail in the deformed shapes. Consequently, even if scaled to 8 × 8, the surface complexity of the deformations remains limited.

The device in[80] Fig. 3o employs the same actuation and control principles as the previous example, resulting in similar performance at the material and system levels. However, it lacks feedback and optimization algorithms to enhance control accuracy. Additionally, it is limited to a 4 × 4 scale, which slightly reduces its surface complexity. Both this

Table 2 | Non-quantifiable characteristics for programmable shape-morphing devices

Inverse control	Continuous–discrete	Feedback	Potential applications	Ref.
No	Continuous	No	–	72 (Fig. 3i)
No	Continuous	No	Adaptive surfaces	73 (Fig. 3j)
No	Continuous	No	Pipeline inspection robots	85 (Fig. 3k)
No	Continuous	No	Human–robot interactions	74 (Fig. 3l)
No	Continuous	No	Tactile displays	79 (Fig. 3m)
Yes	Continuous	Yes	Adaptive surfaces	75 (Fig. 3n)
No	Continuous	No	Advanced optics	80 (Fig. 3o)
Yes	Continuous	No	Tangible use interfaces for AR–VR	76 (Fig. 3p)
Yes	Continuous	Yes	Haptic devices	77
No	Continuous	Yes	Tangible interactive surfaces	81
No	Discrete	No	Tactile displays	88
Yes	Discrete	Yes	3D displays–remote object manipulation	67
Yes	Discrete	Yes	3D displays–haptic devices	65
No	Discrete	Yes	3D displays	66
No	Discrete	No	Transporting and sorting items	71
No	Discrete	No	3D displays	70

AR, augmented reality; VR, virtual reality.

Perspective

and the previous device are suited for applications requiring rapid response without load, such as advanced optics and adaptive surfaces.

Figure 3p[76] introduces a PSM device based on a 6 × 6 ionic actuator array. Although the ionic actuators perform poorly at the material level in terms of actuation rate and load per weight, their maximum deformation curvature is notable. The standout feature of this work lies in its system-level innovation. By employing passive matrix addressing and utilizing the capacitor-like floating state of ionic actuators to maintain deformations, the device achieves independent control of $N2$ actuators using only $2N$ inputs. This setup ensures an actuation decoupling score very close to 1. Combined with the bidirectional continuous large-angle movement of the ionic actuators, this results in the highest surface complexity among all examples.

Because publications often report relatively few metrics, we estimated many of the metrics in the radar charts in Fig. 3.

A standardized evaluation for programmable shape-morphing devices

PPSM entails transitioning from one predefined shape to another. Continuous PSM devices are an emerging device category that allows one device to deform to a continuum of shapes based on different control inputs. This budding arena faces an important challenge: the lack of a standardized evaluation metric. Current assessments of these devices are often subjective and qualitative, making it difficult to compare different technologies in this field. More established fields such as image recognition have standard data sets[98], which allows researchers to directly compare the performance of their devices or algorithms.

To address this gap, we propose a parametric surface as a standard for evaluating PSM devices (Fig. 5). This surface is expressed as:

$$z = H \times \cos(\mathbf{n}_1 \times \pi \times x) \times \cos(\mathbf{n}_2 \times \pi \times y),$$

in which $x, y \in [-1, 1]$.

When either $\mathbf{n}_1$ or $\mathbf{n}_2$ is zero, the surface exhibits unidirectional wave patterns. However, when both $\mathbf{n}_1$ and $\mathbf{n}_2$ are non-zero positive real numbers, it transforms into a bidirectional wavy surface, replete with peaks and valleys.

We suggest this surface as a standard because of its versatility. The parameters $\mathbf{n}_1$ and $\mathbf{n}_2$ intuitively represent the resolution of the shape-morphing device in the x and y directions, respectively. Meanwhile, H represents the maximum bending angle of an actuating segment.

Furthermore, these parameters are intricately linked with a metric discussed earlier: the variance of normal vectors. This is a measure of surface complexity. Even a slight variation in one of these parameters can cause a noticeable change in the variance of normal vectors, highlighting the intricacy or simplicity of the resultant morphed shape.

To illustrate the application of this parametric surface, the values of the parameters are approximated to reproduce deformed shapes reported in recent publications on PSM devices:

(1) ref. 74 presents a dome surface that can be approximated by $H = 0.45$, $\mathbf{n}_1 = 1$ and $\mathbf{n}_2 = 1$. The surface complexity of this device is 3.644.
(2) ref. 75 presents a complex surface akin to parameters $H = 0.15$, $\mathbf{n}_1 = 2$ and $\mathbf{n}_2 = 2$, giving a surface complexity of 6.262.
(3) ref. 76 reports a surface that can be approximated with parameters $H = 0.15$, $\mathbf{n}_1 = 3$ and $\mathbf{n}_2 = 3$. The surface complexity of this structure is 31.201.

Explicitly stating the capabilities of a device in terms of the H, $\mathbf{n}_1$ and $\mathbf{n}_2$ parameters associated with the proposed parametric surface would ensure a more quantitative approach for evaluating advancements in the field of PSM devices.

Shape-morphing devices inevitably exhibit differences from their target shape. The most common way to report these differences is using the absolute value of the error in one or more dimensions[75,76]. However, this absolute error depends on the size of the device and the magnitude of the target deformations. Normalizing the error to the maximum deformation in the out-of-plane direction[82] provides a more robust method of comparison.

Conclusion

The field of shape-morphing devices stands at an exciting crossroads, with potential applications across diverse disciplines. The versatility of these devices, especially in the AR and VR and biomedical sectors, has ignited a growing interest in their development and optimization.
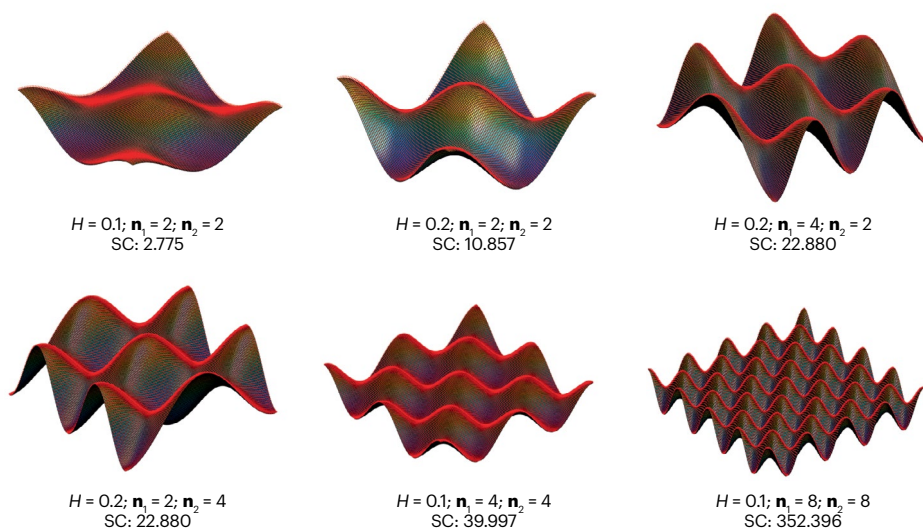

Fig. 5 | Proposed reference parametric surfaces. Proposed parametric surfaces with different parameter inputs and surface complexity (SC) for quantifying the programmability of programmable shape-morphing devices.

$H = 0.1$; $\mathbf{n}_1 = 2$; $\mathbf{n}_2 = 2$
SC: 2.775

$H = 0.2$; $\mathbf{n}_1 = 2$; $\mathbf{n}_2 = 2$
SC: 10.857

$H = 0.2$; $\mathbf{n}_1 = 4$; $\mathbf{n}_2 = 2$
SC: 22.880

$H = 0.2$; $\mathbf{n}_1 = 2$; $\mathbf{n}_2 = 4$
SC: 22.880

$H = 0.1$; $\mathbf{n}_1 = 4$; $\mathbf{n}_2 = 4$
SC: 39.997

$H = 0.1$; $\mathbf{n}_1 = 8$; $\mathbf{n}_2 = 8$
SC: 352.396

Perspective

However, as the field grows, there is a pressing need to establish standardized evaluation systems to objectively compare and benchmark different devices. This Perspective provides a summary of the performance of recently reported shape-morphing devices and introduces a framework for their assessment, paving the way for objective, clear and concise comparisons. In particular, we propose two new methods to quantify the capabilities of shape-morphing systems: a definition of surface complexity based on the variance of normal vectors and a parametric surface that serves as a robust standard. We envision that these frameworks for comparison will be important for understanding the gaps between current technological capabilities and application needs, guiding the development of future technology platforms. As this is the first set of proposed metrics for shape-morphing devices, we expect the community to refine these metrics over time.

References

1. Shah, D. et al. Shape changing robots: bioinspiration, simulation, and physical realization. *Adv. Mater.* **33**, 2002882 (2021).
2. Boston, D. M., Phillips, F. R., Henry, T. C. & Arrieta, A. F. Spanwise wing morphing using multistable cellular metastructures. *Extrem. Mech. Lett.* **53**, 101706 (2022).
3. Sofla, A., Meguid, S., Tan, K. & Yeo, W. Shape morphing of aircraft wing: status and challenges. *Mater. Des.* **31**, 1284–1292 (2010).
4. Abdullah, Y. S. & Al-Alwan, H. A. Smart material systems and adaptiveness in architecture. *Ain Shams Eng. J.* **10**, 623–638 (2019).
5. Sobczyk, M., Wiesenhütter, S., Noennig, J. R. & Wallmersperger, T. Smart materials in architecture for actuator and sensor applications: a review. *J. Intell. Mater. Syst. Struct.* **33**, 379–399 (2022).
6. Walther, A. From responsive to adaptive and interactive materials and materials systems: a roadmap. *Adv. Mater.* **32**, 1905111 (2020).
7. Shahbazi, M., Jäger, H., Ettelaie, R., Mohammadi, A. & Kashi, P. A. Multimaterial 3D printing of self-assembling smart thermo-responsive polymers into 4D printed objects: a review. *Addit. Manuf.* **71**, 103598 (2023).
8. Chen, X. et al. Harnessing 4D printing bioscaffolds for advanced orthopedics. *Small* **18**, 2106824 (2022).
9. Kirillova, A. & Ionov, L. Shape-changing polymers for biomedical applications. *J. Mater. Chem. B* **7**, 1597–1624 (2019).
10. Viola, J. M. et al. Guiding cell network assembly using shape-morphing hydrogels. *Adv. Mater.* **32**, 2002195 (2020).
11. Bertoldi, K., Vitelli, V., Christensen, J. & Van Hecke, M. Flexible mechanical metamaterials. *Nat. Rev. Mater.* **2**, 1–11 (2017).
12. Jiang, S. et al. Flexible metamaterial electronics. *Adv. Mater.* **34**, 2200070 (2022).
13. Jeon, S.-J., Hauser, A. W. & Hayward, R. C. Shape-morphing materials from stimuli-responsive hydrogel hybrids. *Acc. Chem. Res.* **50**, 161–169 (2017).
14. Siéfert, E., Reyssat, E., Bico, J. & Roman, B. Bio-inspired pneumatic shape-morphing elastomers. *Nat. Mater.* **18**, 24–28 (2019).
15. Kim, Y., Yuk, H., Zhao, R., Chester, S. A. & Zhao, X. Printing ferromagnetic domains for untethered fast-transforming soft materials. *Nature* **558**, 274–279 (2018).
    Three-dimensional-printed magnetic-driven pattern-to-pattern shape-morphing device with fast response and high surface complexity.
16. Lin, H.-T., Leisk, G. G. & Trimmer, B. GoQBot: a caterpillar-inspired soft-bodied rolling robot. *Bioinspir. Biomim.* **6**, 026007 (2011).
17. Yim, S. & Sitti, M. Shape-programmable soft capsule robots for semi-implantable drug delivery. *IEEE Trans. Robot.* **28**, 1198–1202 (2012).
18. Han, B. et al. Reprogrammable soft robot actuation by synergistic magnetic and light fields. *Adv. Funct. Mater.* **32**, 2110997 (2022).
19. Li, C. et al. Fast and programmable locomotion of hydrogel–metal hybrids under light and magnetic fields. *Sci. Robot.* **5**, eabb9822 (2020).
20. Wang, J., Chen, G., Zhang, Z., Suo, J. & Wang, H. Wireless multiplexing control based on magnetic coupling resonance and its applications in robot. *J. Mech. Robot.* **14**, 011009 (2022).
21. Xin, C. et al. Environmentally adaptive shape-morphing microrobots for localized cancer cell treatment. *ACS Nano* **15**, 18048–18059 (2021).
22. Wang, C., Wu, Y., Dong, X., Armacki, M. & Sitti, M. In situ sensing physiological properties of biological tissues using wireless miniature soft robots. *Sci. Adv.* **9**, eadg3988 (2023).
23. Wang, J. et al. Pneumatic non-equibiaxial cell stretching device with live-cell imaging. *IEEE Trans. Biomed. Eng.* **71**, 820–830 (2023).
24. Costanza, G. & Tata, M. E. Shape memory alloys for aerospace, recent developments, and new applications: a short review. *Materials* **13**, 1856 (2020).
25. Feng, R. et al. Soft robotic perspective and concept for planetary small body exploration. *Soft Robot.* **9**, 889–899 (2022).
26. Kretzer, M. *Information Materials: Smart Materials for Adaptive Architecture* (Springer, 2016).
27. Mondal, S. Phase change materials for smart textiles — an overview. *Appl. Therm. Eng.* **28**, 1536–1550 (2008).
28. Chai, J. et al. Thermoregulatory clothing with temperature-adaptive multimodal body heat regulation. *Cell Rep. Phys. Sci.* **3**, 100958 (2022).
29. Ford, M. J. et al. A multifunctional shape-morphing elastomer with liquid metal inclusions. *Proc. Natl Acad. Sci. USA* **116**, 21438–21444 (2019).
30. Kotikian, A., Truby, R. L., Boley, J. W., White, T. J. & Lewis, J. A. 3D printing of liquid crystal elastomeric actuators with spatially programmed nematic order. *Adv. Mater.* **30**, 1706164 (2018).
31. Yu, C. et al. Electronically programmable, reversible shape change in two- and three-dimensional hydrogel structures. *Adv. Mater.* **25**, 1541–1546 (2013).
32. Banerjee, H., Suhail, M. & Ren, H. Hydrogel actuators and sensors for biomedical soft robots: brief overview with impending challenges. *Biomimetics* **3**, 15 (2018).
33. Nojoomi, A., Arslan, H., Lee, K. & Yum, K. Bioinspired 3D structures with programmable morphologies and motions. *Nat. Commun.* **9**, 3705 (2018).
34. Zhang, M. et al. Hydrogel muscles powering reconfigurable micro-metastructures with wide-spectrum programmability. *Nat. Mater.* **22**, 1243–1252 (2023).
35. Seffen, K. Mechanical memory metal: a novel material for developing morphing engineering structures. *Scr. Mater.* **55**, 411–414 (2006).
36. Neville, R. M. et al. A kirigami shape memory polymer honeycomb concept for deployment. *Smart Mater. Struct.* **26**, 05LT03 (2017).
37. Mao, Y. et al. 3D printed reversible shape changing components with stimuli responsive materials. *Sci. Rep.* **6**, 24761 (2016).
38. Wu, J. et al. Multi-shape active composites by 3D printing of digital shape memory polymers. *Sci. Rep.* **6**, 24224 (2016).
39. Liu, X. et al. Recent advances in stimuli-responsive shape-morphing hydrogels. *Adv. Funct. Mater.* **32**, 2203323 (2022).
40. Wang, E., Desai, M. S. & Lee, S.-W. Light-controlled graphene–elastin composite hydrogel actuators. *Nano Lett.* **13**, 2826–2830 (2013).
41. Lee, E., Kim, D., Kim, H. & Yoon, J. Photothermally driven fast responding photo-actuators fabricated with comb-type hydrogels and magnetite nanoparticles. *Sci. Rep.* **5**, 15124 (2015).
42. Chen, J., Jiang, J., Weber, J., Gimenez-Pinto, V. & Peng, C. Shape morphing by topological patterns and profiles in laser-cut liquid crystal elastomer kirigami. *ACS Appl. Mater. Interfaces* **15**, 4538–4548 (2023).
43. White, T. J. & Broer, D. J. Programmable and adaptive mechanics with liquid crystal polymer networks and elastomers. *Nat. Mater.* **14**, 1087–1098 (2015).
44. Alapan, Y., Karacakol, A. C., Guzelhan, S. N., Isik, I. & Sitti, M. Reprogrammable shape morphing of magnetic soft machines. *Sci. Adv.* **6**, eabc6414 (2020).
45. Sun, Y. et al. Design and fabrication of a shape-morphing soft pneumatic actuator: soft robotic pad. In *2017 IEEE/RSJ International Conference on Intelligent Robots and Systems (IROS)* 6214–6220 (IEEE, 2017).
46. Choi, G. P., Dudte, L. H. & Mahadevan, L. Programming shape using kirigami tessellations. *Nat. Mater.* **18**, 999–1004 (2019).
47. Overvelde, J. T., Weaver, J. C., Hoberman, C. & Bertoldi, K. Rational design of reconfigurable prismatic architected materials. *Nature* **541**, 347–352 (2018).
48. Xu, T., Zhang, J., Salehizadeh, M., Onaizah, O. & Diller, E. Millimeter-scale flexible robots with programmable three-dimensional magnetization and motions. *Sci. Robot.* **4**, eaav4494 (2019).
49. Barnes, M. et al. Reactive 3D printing of shape-programmable liquid crystal elastomer actuators. *ACS Appl. Mater. Interfaces* **12**, 28692–28699 (2020).
50. Kotikian, A. et al. Untethered soft robotic matter with passive control of shape morphing and propulsion. *Sci. Robot.* **4**, eaax7044 (2019).
51. Boley, J. W. et al. Shape-shifting structured lattices via multimaterial 4D printing. *Proc. Natl Acad. Sci. USA* **116**, 20856–20862 (2019).
    Three-dimensional multimaterial-printed thermal-induced pattern-to-pattern shape-morphing device assembled by bending lattices with high surface complexity.
52. Sydney Gladman, A., Matsumoto, E. A., Nuzzo, R. G., Mahadevan, L. & Lewis, J. A. Biomimetic 4D printing. *Nat. Mater.* **15**, 413–418 (2016).
53. Davidson, Z. S. et al. Monolithic shape-programmable dielectric liquid crystal elastomer actuators. *Sci. Adv.* **5**, eaay0855 (2019).
54. Guo, Y., Zhang, J., Hu, W., Khan, M. T. A. & Sitti, M. Shape-programmable liquid crystal elastomer structures with arbitrary three-dimensional director fields and geometries. *Nat. Commun.* **12**, 5936 (2021).
55. Stanley, A. A. *Haptic Jamming: Controllable Mechanical Properties in a Shape-Changing User Interface* (Stanford University, 2016).
56. Klemmer, S. R., Hartmann, B. & Takayama, L. How bodies matter: five themes for interaction design. In *Proc. 6th Conference on Designing Interactive systems* 140–149 (ACM, 2006).
57. Urbas, A. M. et al. Roadmap on optical metamaterials. *J. Opt.* **18**, 093005 (2016).
58. Chen, Y., Ai, B. & Wong, Z. J. Soft optical metamaterials. *Nano Converg.* **7**, 18 (2020).
59. Cummer, S. A., Christensen, J. & Alù, A. Controlling sound with acoustic metamaterials. *Nat. Rev. Mater.* **1**, 16001 (2016).
60. Wenz, F. et al. Designing shape morphing behavior through local programming of mechanical metamaterials. *Adv. Mater.* **33**, 2008617 (2021).
61. Peng, C. *Dynamically Programmable Surfaces for High-Speed Optical Modulation and Detection* (Massachusetts Institute of Technology, 2020).
62. Zhang, Z. & Krushynska, A. Programmable shape-morphing of rose-shaped mechanical metamaterials. *APL Mater.* https://doi.org/10.1063/5.0099323 (2022).

Perspective

63. Liu, C. et al. Programmable mechanical metamaterials: basic concepts, types, construction strategies — a review. *Front. Mater.* **11**, 1361408 (2024).

64. Hirota, K. & Hirose, M. Surface display: concept and implementation approaches. In *Proc. Fifth Int. Conf. Artificial Reality and Tele-Existence* 185–192 (ACM-SIGCHI, 1995).

65. Iwata, H., Yano, H., Nakaizumi, F. & Kawamura, R. Project FEELEX: adding haptic surface to graphics. In *Proc. 28th Annual Conference on Computer Graphics and Interactive Techniques* 469–476 (ACM, 2001).

66. Leithinger, D. & Ishii, H. Relief: a scalable actuated shape display. In *Proc. Fourth International Conference on Tangible, Embedded, and Embodied Interaction* 221–222 (ACM, 2010).

67. Follmer, S., Leithinger, D., Olwal, A., Hogge, A. & Ishii, H. inFORM: dynamic physical affordances and constraints through shape and object actuation. In *Proc. 26th Annual ACM Symposium on User Interface Software and Technology* (*UIST*) 417–426 (ACM, 2013).

68. Zhu, H. & Book, W. J. Practical structure design and control for digital clay. In *ASME International Mechanical Engineering Congress and Exposition* 1051–1058 (ASME, 2004).

69. Deng, Z., Stommel, M. & Xu, W. A novel soft machine table for manipulation of delicate objects inspired by caterpillar locomotion. *IEEE/ASME Trans. Mechatron.* **21**, 1702–1710 (2016).

70. Poupyrev, I., Nashida, T., Maruyama, S., Rekimoto, J. & Yamaji, Y. Lumen: interactive visual and shape display for calm computing. In *ACM SIGGRAPH 2004 Emerging Technologies* Vol. 17 (2004).

71. Wang, T., Zhang, J., Hong, J. & Wang, M. Y. Dielectric elastomer actuators for soft wave-handling systems. *Soft Robot.* **4**, 61–69 (2017).

72. Coelho, M., Ishii, H. & Maes, P. Surflex: a programmable surface for the design of tangible interfaces. In *CHI'08 Extended Abstracts on Human Factors in Computing Systems* 3429–3434 (2008).

73. Yang, B. et al. Reprogrammable soft actuation and shape-shifting via tensile jamming. *Sci. Adv.* **7**, eabh2073 (2021).

74. Liu, K., Hacker, F. & Daraio, C. Robotic surfaces with reversible, spatiotemporal control for shape morphing and object manipulation. *Sci. Robot.* **6**, eabf5116 (2021). **Programmable shape-morphing device that uses three liquid crystal elastomer bending actuators oriented along each of two orthogonal directions with high load per weight.**

75. Bai, Y. et al. A dynamically reprogrammable surface with self-evolving shape morphing. *Nature* **609**, 701–708 (2022). **Programmable shape-morphing device driven by the Lorentz force from magnetic fields, comprising 8×8 interconnected, serpentine-shaped beams made of thin conductive layers.**

76. Wang, J., Sotzing, M., Lee, M. & Chortos, A. Passively addressed robotic morphing surface (PARMS) based on machine learning. *Sci. Adv.* **9**, eadg8019 (2023). **Highly under-actuated programmable shape-morphing device made by 6×6 ionic actuator arrays controlled by a machine-learning algorithm.**

77. Stanley, A. A., Hata, K. & Okamura, A. M. Closed-loop shape control of a Haptic Jamming deformable surface. In *IEEE Int. Conf. Robotics and Automation* (*ICRA*) 2718–2724 (IEEE, 2016).

78. Devlin, M. R. et al. Soft, modular, shape-changing displays with hyperelastic bubble arrays. In *IEEE/RSJ Int. Conf. Intelligent Robots and Systems* (*IROS*) 5101–5106 (IEEE, 2023).

79. Rauf, A. M., Bernardo, J. S. & Follmer, S. Electroadhesive auxetics as programmable layer jamming skins for formable crust shape displays. In 2023 *IEEE Int. Conf. Robotics and Automation* (*ICRA*) 2591–2597 (IEEE, 2023).

80. Ni, X. et al. Soft shape-programmable surfaces by fast electromagnetic actuation of liquid metal networks. *Nat. Commun.* **13**, 5576 (2022).

81. Tsimeris, J., Dedman, C., Broughton, M. & Gedeon, T. ForceForm: a dynamically deformable interactive surface. In *Proc. 2013 ACM International Conference on Interactive Tabletops and Surfaces* 175–178 (ACM, 2013).

82. Hajiesmaili, E., Larson, N. M., Lewis, J. A. & Clarke, D. R. Programmed shape-morphing into complex target shapes using architected dielectric elastomer actuators. *Sci. Adv.* **8**, eabn9198 (2022).

83. Shah, D. S., Yang, E. J., Yuen, M. C., Huang, E. C. & Kramer-Bottiglio, R. Jamming skins that control system rigidity from the surface. *Adv. Funct. Mater.* **31**, 2006915 (2021).

84. Pikul, J. H. et al. Stretchable surfaces with programmable 3D texture morphing for synthetic camouflaging skins. *Science* **358**, 210–214 (2017). **Pneumatic pattern-to-pattern shape-morphing device based on bulking deformation with fast inverse design and fabrication.**

85. Steltz, E., Mozeika, A., Rodenberg, N., Brown, E. & Jaeger, H. M. JSEL: jamming skin enabled locomotion. In 2009 *IEEE/RSJ Int. Conf. Intelligent Robots and Systems* 5672–5677 (IEEE, 2009).

86. Kim, J., Hanna, J. A., Hayward, R. C. & Santangelo, C. D. Thermally responsive rolling of thin gel strips with discrete variations in swelling. *Soft Matter* **8**, 2375–2381 (2012).

87. Hauser, A. W., Evans, A. A., Na, J. H. & Hayward, R. C. Photothermally reprogrammable buckling of nanocomposite gel sheets. *Angew. Chem.* **127**, 5524–5527 (2015).

88. Velazquez, R., Pissaloux, E., Hafez, M. & Szewczyk, J. A low-cost highly-portable tactile display based on shape memory alloy micro-actuators. In *IEEE Symp. Virtual Environments, Human–Computer Interfaces and Measurement Systems* (IEEE, 2005).

89. Zhang, J. et al. Robotic artificial muscles: current progress and future perspectives. *IEEE Trans. Robot.* **35**, 761–781 (2019).

90. Traugutt, N. A. et al. Liquid-crystal-elastomer-based dissipative structures by digital light processing 3D printing. *Adv. Mater.* **32**, 2000797 (2020).

91. McConney, M. E. et al. Topography from topology: photoinduced surface features generated in liquid crystal polymer networks. *Adv. Mater.* **25**, 5880–5885 (2013). **Photo-activated pattern-to-pattern shape-morphing device with multiple deformation patterns under different light wavelengths based on liquid crystal elastomer networks.**

92. Mac Murray, B. C. et al. Compliant buckled foam actuators and application in patient-specific direct cardiac compression. *Soft Robot.* **5**, 99–108 (2018).

93. Takei, K. et al. Nanowire active-matrix circuitry for low-voltage macroscale artificial skin. *Nat. Mater.* **9**, 821–826 (2010).

94. Bao, B., Karnaushenko, D. D., Schmidt, O. G., Song, Y. & Karnaushenko, D. Active matrix flexible sensory systems: materials, design, fabrication, and integration. *Adv. Intell. Syst.* **4**, 2100253 (2022).

95. Wang, S. et al. Skin electronics from scalable fabrication of an intrinsically stretchable transistor array. *Nature* **555**, 83–88 (2018).

96. Wang, J. & Chortos, A. Control strategies for soft robot systems. *Adv. Intell. Syst.* **4**, 2100165 (2022).

97. Laschi, C. & Mazzolai, B. Lessons from animals and plants: the symbiosis of morphological computation and soft robotics. *IEEE Robot. Autom. Mag.* **23**, 107–114 (2016).

98. Ambrogio, S. et al. Equivalent-accuracy accelerated neural-network training using analogue memory. *Nature* **558**, 60–67 (2018).

Competing interests
The authors declare no competing interests.

Additional information
Peer review information *Nature Reviews Materials* thanks Rebecca Kramer-Bottiglio and the other, anonymous, reviewer(s) for their contribution to the peer review of this work.

Publisher's note Springer Nature remains neutral with regard to jurisdictional claims in published maps and institutional affiliations.